ARTICLE

The Interaction of Supramolecular Anticancer Drug Amphiphiles with Phospholipid Membranes

Received 00th January 20xx, Accepted 00th January 20xx

DOI: 10.1039/x0xx00000x

Phu K. Tang^{†,a,b}, Anjela Manandhar^{†,a,b}, William Hu^c, Myungshim Kang^a, Sharon M. Loverde^{a,b,c,d}

16

17

33

34

)

The shape of drug delivery vehicles impacts both the circulation time and the effectiveness of the vehicle. Peptide-based drug amphiphiles (DAs) are promising new candidates as drug delivery vehicles that can self-assemble into shapes such as nanofilament and nanotube (diameter $^{\sim}$ 6-10 nm). The number of conjugated drugs affects the IC50 of these DAs, which is correlated to the effective cellular uptake. Characterizing and optimizing the interaction of these DAs and their assemblies with the cellular membrane is experimentally challenging. Long-time molecular dynamics can determine if the DA molecular structure affects the translocation across and interaction with the cellular membrane. Here, we report long-time atomistic simulation on Anton 2 (up to 25 μ s) of these DAs with model cellular membranes. Results indicate that the interaction of these DAs with model cellular membranes is dependent on the number of conjugated drugs. We find that, with increased drug loading, the hydrophobic drug (camptothecin) builds up in the outer hydrophobic core of the membrane, pulling in positively charged peptide groups. Next, we computationally probe the interaction of differing shapes of these model drug delivery vehicles—nanofilament and nanotube—with the same model membranes, finding that the interaction of these nanostructures with the membrane may play a key role in modulating the interaction between the nanostructure and the membrane may play a key role in modulating the interaction between the nanostructure and the membrane. Taken together, these results offer important insights for the rational design of peptide-based drug delivery vehicles.

Introduction

1

2

3

4

5

6

7

8

9

10

11

14

15

There are many challenges in the design of an effective dryg delivery vehicle, including a controlled and high drug loading capacity, extending the circulation time in blood-stream¹, eliminating non-specific cell uptake², tunability of the vehicle morphology/shape at the nanoscale³, and ultimately control of the vehicle interactions with the cellular membrane—either through active targeting the cellular receptors and/or control of the membrane response the morphology⁴ and/or surface patterning⁵, ⁶. Small molecules such the polarity, can cross the membrane via a passive diffusion or else the proteins and viruses (≥ 10 kDa) traverse the membrane barrier eith through pore formation or endocytosis⁶. The relative contributions to the free energy of interaction between the particle (large)

molecule such as protein or virus) and the membrane include the bending energy of the membrane, the membrane tension, as well as any adhesive contact between the particle and membrane⁹. Particle-based simulation methods such as molecular dynamics offer an emerging tool to probe nanoparticle-membrane interactions^{10, 11}, characterizing, for example, the effect of size¹², shape¹³, surface charge¹⁴, and chemistry of the nanoparticle¹⁵. For example, molecular simulations can uniquely capture deformations and rearrangements of the nanoparticle itself at the molecular level, such as molecular 'snorkeling' 15, which cannot be well-described with continuum models. Ultimately, design of an effective drug delivery vehicle entails engineering not only the shape of the vehicle, but the interaction with the cellular membrane.

Peptide amphiphiles (PAs) are a class of peptide-based molecules composed of hydrophilic head and hydrophobic tail 16-18 that selfassemble into ordered nanostructures of various morphologies, such as ribbons, bilayers, tubes, and fibers 19-22. The morphology of the self-assembled nanostructure is driven at the molecular level by the balance of hydrophobicity and hydrophilicity, which can be further tuned by the peptide sequence. Peptide sequence can be tailored for various biomedical purposes such as stabilizing membrane proteins^{23, 24}, facilitating cell differentiation²⁵, as well as serving as drug delivery vehicles^{26, 27}. Indeed, peptides, such as 'cellpenetrating peptides' or CPPs, are classic examples of molecules that can be tailored via sequence to affect their membrane interaction. For example, certain functional domains²⁸ control the translocation activity²⁹. As a result, these findings also act as general guidelines for rational designs of CPPs as potent drug delivery tools³⁰⁻³². Additionally, CPPs, such as a non β -sheet forming peptide from the protein transduction domain of Tat, HIV protein³³, can also be coupled to hydrophobic drugs to improve their delivery

Electronic Supplementary Information (ESI) available: [Figures S1-S5 contain the average cluster sizes and number of clusters over time for mCPT and qCPT, the local thickness profiles of the POPC membrane over time as well as locations of 8 drugs that penetrate the membrane over time, hydrogen bonds over time for the 'mCPT-1 buSS-Tau' system, density profile of nanostructure-membrane contact interface for the last umbrella sampling window, average hydrogen bonds between the nanofilament/nanotube and the membrane]. See DOI: 10.1039/x0xx00000x

^{a.} Department of Chemistry, College of Staten Island, City University of New York, 2800 Victory Blvd., 65-238, Staten Island, NY 10314

b. Ph.D. Program in Biochemistry, The Graduate Center of the City University of New 7 York, New York, United States

^{c.} Hunter College High School, New York, NY 10128

d. Ph.D. Program in Chemistry and Physics, The Graduate Center of the City University of New York, New York, United States

[†] Co-first authors

effectiveness³⁴. For example, *Cui et al.*³⁵ designed peptide-bas dd drug amphiphiles (DAs), consisting of a short modified Tau peptide sequence (CGVQIVYKK)³⁶—the β-sheet forming segment of Tdd (protein that stabilizes microtubules³⁷)— and hydrophoblic anticancer drug camptothecin (CPT), conjugated via a biodegradable disulfide linker (buSS)^{38, 39} as shown in **Figure 1 A** and **B**. Tdd sequence, CGVQIVYKK, is derived from a model peptide sequente (VQIVYK) that forms both parallel and anti-parallel β-sheets been used in constructing peptide amphiphiles as reviewed 2d Manandhar et al.⁴⁰ Indeed, drug conjugates that employ disulfide

2

3

4

5

6

7

8

9

10

bonds can be reduced at varying locations within cells³⁸. Nonetheless, conventional MD simulations cannot take into account the reversible dynamics of the disulfide bonds. CPT is a model hydrophobic anticancer drug⁴¹ with a known octanol/water partition coefficient⁴², ⁴³ that can π - π stack in solution due to its planar aromatic structure⁴⁴, driving the self-assembly process. Dependent on the molecular structure of the DAs, such as the number of conjugated drugs ('mCPT' or 'mCPT-buSS-Tau', which has one drug attached, vs. 'qCPT' or 'qCPT-buSS-Tau', which has four drugs attached), the shape of the self-assembly in solution ranges from nanofilament (diameter ~ 6.5 nm) to nanotube (diameter ~ 9.5 nm)³⁵.

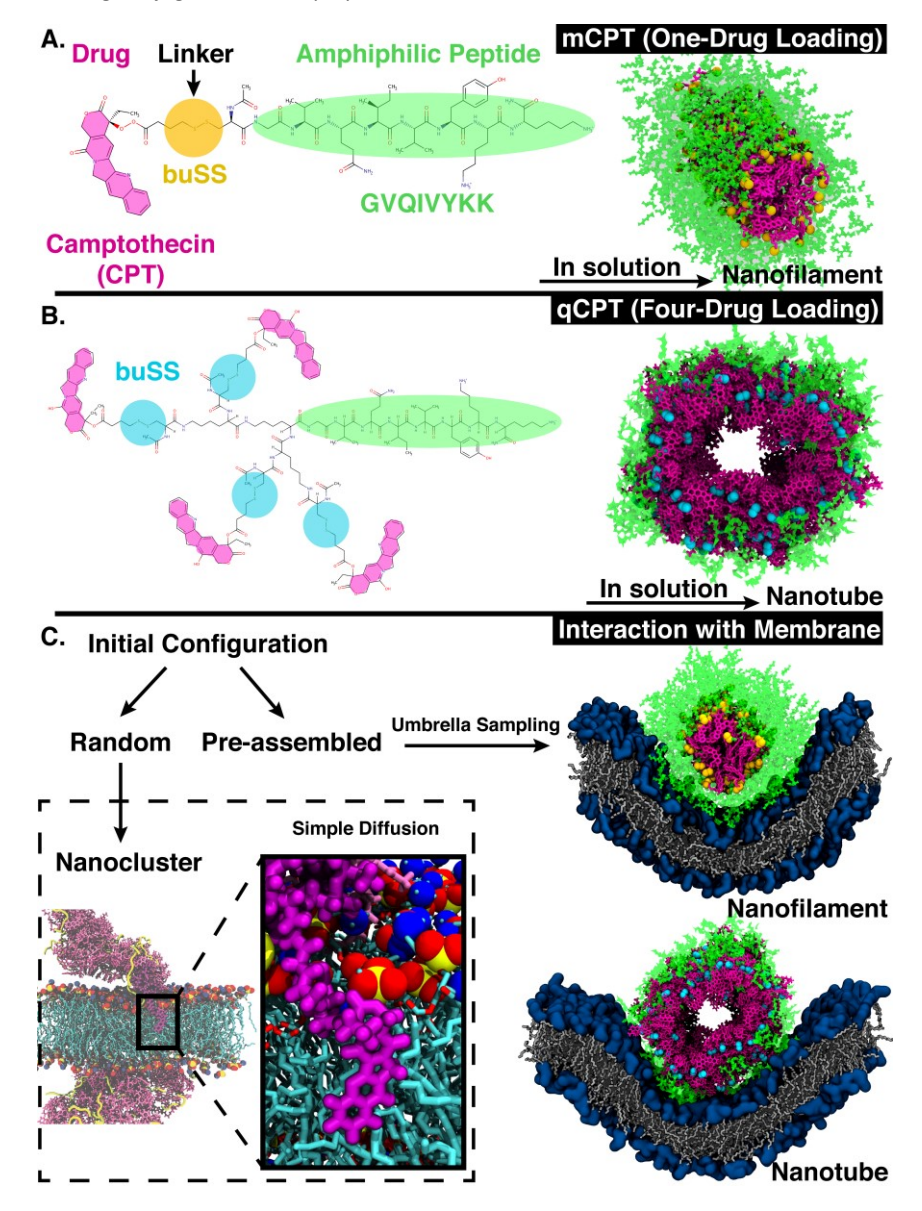


Figure 1. A. Chemical structure of 'mCPT-buSS-Tau', which has one-drug loaded per peptide. In solution, 'mCPT-buSS-Tau' can self-assemble into a nanofilament. Camptothecin (CPT), Linker, and Peptide are highlighted in magenta, yellow, and green, respectively. **B.** Chemical structure of 'qCPT-buSS-Tau'. In solution 'qCPT-buSS-Tau' can self-assemble into a nanotube. CPT, Linker, and Peptide are highlighted in magenta, blue, and green, respectively. **C.** Random initial configurations of 'mCPT-buSS-Tau' and 'qCPT-buSS-Tau' interact with a model membrane using unbiased molecular dynamics simulations (or simple diffusion). CPT (in magenta) and peptide (in yellow) are shown in 'Licorice' and 'New Cartoon' representation, respectively. The zoomed-in view shows a insertion of CPT into the model POPC (1-palmitoyl-2-oleoyl-sn-glycero-3-phosphocholine) membrane (head groups: van der Waals representation, colors: choline (blue) and phosphate (red, yellow)). Pre-assembled initial configurations of the nanofilament and the nanotube interact with the membrane using Umbrella Sampling. The head groups of the membrane are represented in dark blue 'QuickSurf' representation and the grey acyl tails in

Journal Name ARTICIF

62

63

64

Essentially, varying the drug loading varies the relative balance 44 hydrophobic to hydrophilic interactions, which determines tA6 relative shape and diameter of these unidimensional self-assembliæ6

In this article, we computationally investigate the dynamic seff. assembly and stability of peptide-drug amphiphiles (DAs), as well 48 characterize their interactions with a model cellular membrane. W49 find that with increased drug loading singular DAs penetrate t50 membrane at short time scales (0.5 µs) due to their increas 51 hydrophobicity and increased accessibility of the drug (Figure 1 5)2 Using advanced sampling methods in molecular dynamics, we fib3 that self-assembled DA nanostructures—nanofilament abd nanotube—repel the model membrane, forcing the membrane 55 thin and bend. This computational approach can be extended 56 molecularly design further self-assembled drug carriers, as well 57 predict the method of drug transport across the cellular membrar 5-8 With additional molecular design, control of the self-assembly sha 59 and interaction with and transport across the cellular membrane 60 these DA's can then be optimized.

Computational Methods

2

3

4

5

6

7

8

9

10

11

12

13

14

15

16

17

18

19

20

21

22

23

24

25

26

27

28

29

30

33

34

35

36

37

38

39

40

41

42

System Setups. The phospholipid bilayers were preassembled and minimized using CHARMM-GUI⁴⁵. The 1-palmitoyl-2-oleoyl-sa glycero-3-phosphocholines or POPC phospholipids parameterized using the Amber Lipid14⁴⁶ force field. Next, the bilayer was further equilibrated, in NAMD 2.1347, with an anisotropio Langevin barostat^{48, 49} using an oscillation period and decay time **9**1 100 fs and 50 fs, respectively, for ~100ns. A damping coefficient of $\sqrt{5}$ =1 ps⁻¹, at a pressure of 1 atm, was used together with the Lange $\frac{1}{3}$ barostat to allow fluctuations of the membrane. 'mCPT-buSS-Taay'4 and 'qCPT-buSS-Tau' were parameterized with the General Amber Force Field (GAFF)⁵⁰. TIP3P water was used. Packmol⁵¹ was used set-up the initial configuration where the DAs were placed randomly above and below the POPC bilayer membrane. The 'mCPT-buSS-Tau' and 'qCPT-buSS-Tau' with POPC membrane systems were equilibrated for 80 ns and 88 ns respectively. nanofilament/nanotube systems were constructed by combining 70 pre-equilibrated POPC membrane and the 'mCPT-buSS-Tago' nanofilament or the 'qCPT-buSS-Tau' nanotube. The nanofilament was constructed in the same way as previous nanofilaments reported by Kang et al. 52 , specifically the nanotube where all four CPT drugs are parallel to each other. All systems used tleap from AmberTool ఖేస్తే to neutralize the overall charge with Cl⁻ions. All system details/sizes are listed in Table 1.

Table 1. System details/sizes.

Table 1. System details/ Sizes.							
Initial	Random		Pre-assembled				
Configuration							
System	mCPT	qCPT	Nanofilament	Nanotube			
Box Size, Å ³	127×	128×126	160 × 158 ×	123 × 196			
	131 ×	×143	207	× 210			
	177						
Molecules of	500	500	505	505			
POPC							
Molecules of	72,929	46,000	90,916	87,089			
Water							
Molecules of	54	108	336	144			
Cl-							
Molecules of	54	54	168	72			
DA							
Bulk [DA],	39.3	54.7	N/A	N/A			
mM							

MD Simulation Parameters. All systems used the NPT ensemble with Langevin dynamics^{48, 49} with a temperature of 310 K. A damping coefficient of y =1 ps⁻¹, at a pressure of 1 atm, was used together with an anisotropic barostat to allow fluctuations of the membrane with a piston period of 100 fs and a damping time scale of 50 fs. The SHAKE algorithm⁵⁴ was used to fix hydrogen atoms allowing a 2 fs timestep. The Particle Mesh Ewald (PME) algorithm55 was utilized to take full electrostatic interactions into account, with full periodic boundary conditions. The cut-off for van der Waals interactions was 12 Å with a smooth switching function at 10 Å. Bonded atoms were excluded from non-bonded atom interactions using a scaled 1-4 value. After equilibration, all random systems were transferred to Anton 2⁵⁶ for production runs. During production runs on Anton 2, the timestep was changed to 2.5 fs. The short-range electrostatics was calculated every timestep while the long-range electrostatics was calculated every three timesteps. The Gaussian Split Ewald method⁵⁷ was used to accelerate the electrostatic calculations. All other parameters used suggested by the Anton2 website were as (wiki.psc.edu/twiki/viewauth/Anton/WebHome). A production run of 18 µs was performed for the 'mCPT-buSS-Tau'-POPC system and 25 μs for the 'qCPT-buSS-Tau'-POPC system.

Umbrella Sampling. Here, we use Umbrella Sampling (US)58 to determine the interaction free energy of the 'mCPT-buSS-Tau' nanofilament and the 'qCPT-buSS-Tau' nanotube with the POPC membrane. US is one of the widely used method to calculate free energy for various biophysical properties such as -protein folding^{59,} ⁶⁰, peptide-peptide interactions^{61, 62}, peptide-DNA interactions⁶³, and peptide-membrane interactions⁶⁴. The reaction coordinate (r_c) is the z-distance between the center of mass of the nanofilament/nanotube and the membrane which is divided into multiple windows. For each US window a biasing harmonic potential (w_i) is applied such that the states samples near the center of the window. The w_i in each window is defined as

$$w_i = \frac{K}{2}[Q - q_i]^2$$
 [Eq. 1]

 $w_i = \frac{K}{2}[Q-q_i]^2 \qquad \qquad \text{[Eq. 1]},$ where k is the spring constant, q_i is the center and Q is the actual difference of r_c for initial and final state. The biased distribution function for every ih window is defined as

$$\langle p(\xi) \rangle_i^{biased} = e^{-w_i(\xi)/k_B T} \langle p(\xi) \rangle \langle e^{-w_i(\xi)/k_B T} \rangle^{-1}$$
 [Eq. 2],

and the unbiased PMF is defined as

$$W_i(\xi) = -k_B T \times \ln(p(\xi)) - w_i + -F_i$$
 [Eq. 3],

where F_i is the unknown free energy constant, defined as

$$e^{F_i/k_BT} = \langle e^{w_i/k_BT} \rangle$$
 [Eq. 4],

47

48

49

50

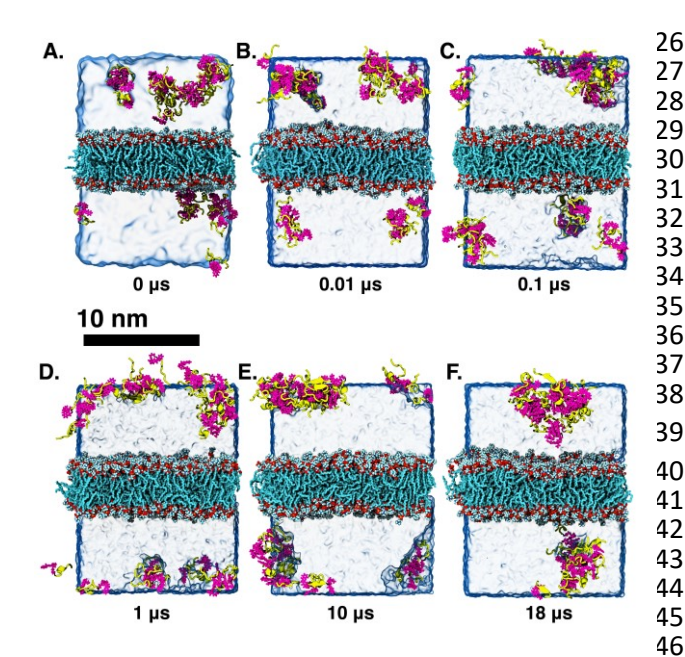


Figure 2. A. - F. Snapshots along the 18 microsecond trajectory showing nanoclusters of 'mCPT-buSS-Tau' interacting with the model **POPC** (1-palmitoyl-2-oleoyl-sn-glycero-3phosphocholine) membrane. CPT (Camptothecin) are in magenta with 'Licorice' representation, peptides are yellow with a 'Secondary Structure' representation. The linkers are in black. POPCs is shown in cyan, red, and white in a 'Licorice' representation. The water is shown with a transparent box.

Next, the weighted histogram analysis method (WHAM)⁶⁵ is used to 2 determine F_i . This uses an iterative process by making initial guess of 3

 F_i to estimate unbiased probability distribution as

$$\langle p(\xi) \rangle = \sum_{i} n_{i} \langle p(\xi) \rangle_{i} \left[\sum_{j} n_{j} e^{\frac{(w_{i}(\xi) - F_{i})}{k_{B}T}} \right]^{-1}$$
 [Eq. 5]

The resulting probability is then used to get new set of F_i values,

 $e^{-F_i/k_BT} = \int d\xi e^{-(w_i(\xi) - F_i)/k_BT} \langle p(\xi) \rangle$

Here, we performed steered MD⁶⁶ (SMD) simulations to pull the nanofilament and the nanotube with 7 kcal/mol force towards the POPC membrane to generate the initial positions in each window. Thus, the nanofilament interaction with the membrane has 38 windows 1Å apart with r_c varying 70.5 Å to 33.5 Å (Figure 7). Similarly, the nanotube interaction with the membrane has 49 windows 1Å apart with r_c varying 84.5 Å to 36.5 Å (Figure 8). Each configuration is harmonically constrained with spring constant of 20kcal/mol. These simulations have periodic boundary conditions, thus infinitely long nanofilament/nanotube is interacting with an infinitely wide cell membrane. For the nanostructure-membrane systems, same MD parameters as that for random drug amphiphile-membrane systems are used.

18 Results

5

6

7

8

9

10

11

12

13

14

15

16

17

19

20

21

22

23

24

25

Low Drug Loading and Interaction with a POPC Membrane.

Long-time molecular dynamics can assess if the DA structure affects the translocation across and interaction with the cellular membrane. To begin with, studies on Anton256 indicate that the interaction of 'mCPT-buSS-Tau' with model cellular membranes is repulsive, and that small aggregates of the DAs do not interact with or disturb the membrane as shown in Figure 2, even after 18 µs simulation time. As

shown in Figure 2, the DAs slowly start to cluster over the 18 μs timeframe, however they do not penetrate or disturb the membrane. 54 'mCPT-buSS-Tau' molecules (39.3 mM) are placed initially randomly above and below a model POPC (1-palmitoyl-2oleoyl-sn-glycero-3-phosphocholine) membrane. Notably, this concentration is about 80-fold higher than the experimental concentration that is reported by Cui et. al.35 At a concentration of 0.05 mM, 'mCPT-buSS-Tau' forms nanofilaments with a 6.7 nm width in solution³⁵. In Figure 2 A-F, snapshots show that 'mCPT-buSS-Tau' nanoclusters form at the early state of the simulation (within the first 0.01 µs) and persist over the course of the simulation. It is known that the $\pi - \pi$ interaction of the aromatic rings on CPT dictate the early nucleation of the DA nanoclusters, according to Kang et. al44. We quantify the average size of nanoclusters as $\frac{\sum_{cluster N_{drug,cluster}}}{\sum_{cluster}}$ However, 'mCPT-buSS-Tau' contains an average of only five drugs per

nanocluster, as shown in Figure 3 A. Moreover, the distribution of sizes of 'mCPT-buSS-Tau' nanoclusters is persistently lower than 'qCPT-buSS-Tau' as shown in Supplemental Figure 1. In other words, 'mCPT-buSS-Tau' prefers to stay in smaller size nanoclusters. Supplemental Figure 1 A-B shows an average of 10 'CPTs' per nanocluster. Furthermore, we also observe that the CPT nanoclusters gradually reach an equilibrium size after 6 μs, with an average of ~10-15 monomers in 3-6 nanoclusters. At 6 and 13 μs, we observe the formation of a 'percolated' nanocluster with all 54 CPTs, but it is not stable and dissolves into smaller size nanoclusters. We

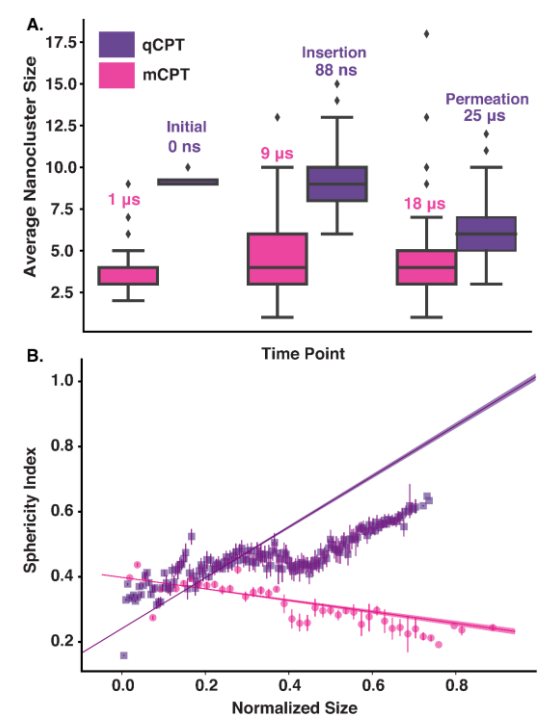


Figure 3. A. The average size of 'mCPT-buSS-Tau' and 'qCPTbuSS-Tau' nanoclusters based on drug aggregation is shown after three time points for 'mCPT-buSS-Tau' (magenta) (1 μs, 9 μs, and 18 μs) and 'qCPT-buSS-Tau' (purple): 'Initial' (0 μ s), 'Insertion' (88 ns), and 'Permeation' (18 μ s). The lowest, middle, and top lines of the boxes are 25, 50, and 75 percentiles, respectively. The top and bottom lines are maxima and minima, with the outliers as black diamonds. B. The sphericity index as a function of normalized size. The error bars are shown as straight lines. Linear regressions with 95% confident interval are shown.

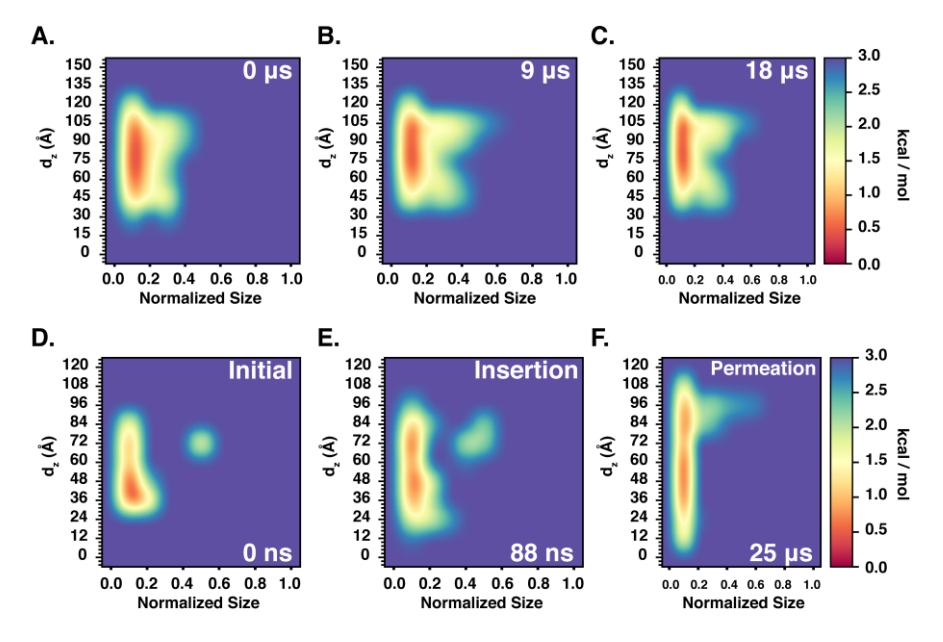


Figure 4. 2D Potential of Mean Force (or PMF) profiles that shows the relationship between normalized nanocluster size and the relative distance, d_z , between the lowest points of 'mCPT-buSS-Tau' (4 A-C. $0 - 18 \mu s$) and 'qCPT-buSS-Tau' (4 D-F $0 - 25 \mu s$) nanoclusters and the center of mass of the model POPC membrane.

define the normalized cluster size as a fraction between 0 and 1 $\frac{35}{N_{drug,cluster}}$. We group the DA molecules that stay within the r_{cut} $\frac{36}{37}$ of 4.5 Å. To quantify the shape of each defined nanocluster, we align each nanocluster's principal axes along x, y, and z direction. The radius of gyration, R, is derived from the principal moment of inertiagonal $I = mR^2$, along one direction of each nanocluster where R is the total mass in grams of each nanocluster. The ratio of minimum radius of gyration, R_{min} , to the maximum radius of gyration, R_{max} , was used to quantify the shape of each nanocluster as the sphericity index R_{max} . Using this index, a spherical aggregate will have a value close to 1. In Figure 3 B, small to medium nanoclusters, which corresponds to R_{min} . O.25 normalized size, have a sphericity index of 0.5. This indicates that small nanoclusters are almost ellipsoidal. Interestingly, large nanoclusters, which reach a normalized size of 0.75, elong and horizontally. This trend is predicted to hold for even large nanoclusters, since the linear regression shows a negative slope. The anisoptropic growth of 'mCPT-buSS-Tau' nanoclusters is supported by Cheetham et. R_{min} and R_{min} and R_{min} and R_{min} and R_{min} are all R_{min} and R_{min} and R_{min} and R_{min} and R_{min} are supported by Cheetham et. R_{min} and R_{min} are supported as R_{min} and R_{min}

1

2

3

5

6

7

8

9

10

11

12

13

14 15

16

17

18

19

20

21

22

23

24

25

26

27

28

29

30

31

nanoclusters, since the linear regression shows a negative slope. The anisoptropic growth of 'mCPT-buSS-Tau' nanoclusters is supported by Cheetham et. al³⁵ and Kang et. al⁴⁴ studies. Furthermore, we also characterize the 2D free energy surfa that correlates the 'mCPT-buSS-Tau' nanocluster sizes and the relative distance, d_z, from the center of mass (COM) of the POPO membrane to the closest point (or closest atom within eaeth nanocluster) of each of the nanoclusters. 2D Potential of Mean For $\frac{1}{2}$ (PMF). The free energy is derived from the distribution probabil $\Re 9$ equatio (A) using $\Delta G = -RT ln\left(\frac{p}{p_{max}}\right)$ where R is the gas law constant, temperature 62 T is in Kelvin and $\frac{p}{p_{max}}$ is the ratio between the probability of a single event to the highest probability event. In Figure 4 A, small 60 medium 'mCPT-buSS-Tau' nanoclusters (~ 0.1-0.4 normaliz nanocluster size) are placed randomly at least 20 Å above the PO 66 membrane. Over the course of 18 μs, those small to medium nanoclusters move further away from the membrane as shown 98 Figure 4 B-C. The free energy minimum is located around 75 to 90 99

with the closest d_z at 30 Å away. Closer observations show that the $\frac{70}{2}$

are two peaks along the normalized size direction corresponding to two distinctive $d_{z'}s$. The first peak with maximum normalized size at 0.4 always stays closer to the membrane, at ~ 45 Å, while the second peak with maximum normalized size at 0.6 is staying further away from the membrane, at ~ 105 Å. Although the overall normalized size mostly remains the same for the two peaks, the trend indicates that small to medium nanoclusters tend to get closer to the membrane. We hypothesize that the positively charged lysines, on the amphiphilic peptides, when aggregating in larger groups will repulse the positively charged choline head groups of the membrane. This repulsion can hinder the normalized size of the nanocluster and may also prevent their approach to the membrane surface. This could also correlate to the lowest *in vitro* efficiency of 'mCPT-buSS-Tau' in cell culture³⁵. However, a definitive answer requires more insightful

Higher Drug Loading and Interaction with a POPC membrane.

Another DA is 'qCPT-buSS-Tau' (Figure 1 B), which carries four times the number of drugs per peptide (four times the drug loading). However, in this case, due to the increased relative accessibility of the CPT, the drug starts to interact with and penetrate the membrane just after 88 ns (Figure 5 B). After 25 μs we see that the drug builds up in a stacking configuration in the outer hydrophobic core of the membrane, starting to bend the membrane, pulling the positively charged peptide groups towards the membrane (Figure 5 C). The electrostatic potential at and surrounding the membrane, before contact with the drugs, during initial drug penetration of the membrane, and after 25 μs, is also shown in Figure 5 D-F. 54 qCPT molecules or 54.7 mM are placed randomly above and under the POPC membrane, same as previously described for the 'mCPT-buSS-Tau'-membrane system. Again, this concentration is approximately 80-fold higher than the concentration that forms 9.5-nm-width nanotubes in TEM and cryo-TEM experiments³⁵. Over a 25-μs simulation, we find more significant interaction of the 'qCPT-buSS-Tau' with the model POPC membrane than with the 'mCPT-buSS-Tau' nanoclusters. Indeed, we find that the 'qCPT-buSS-Tau' nanoclusters

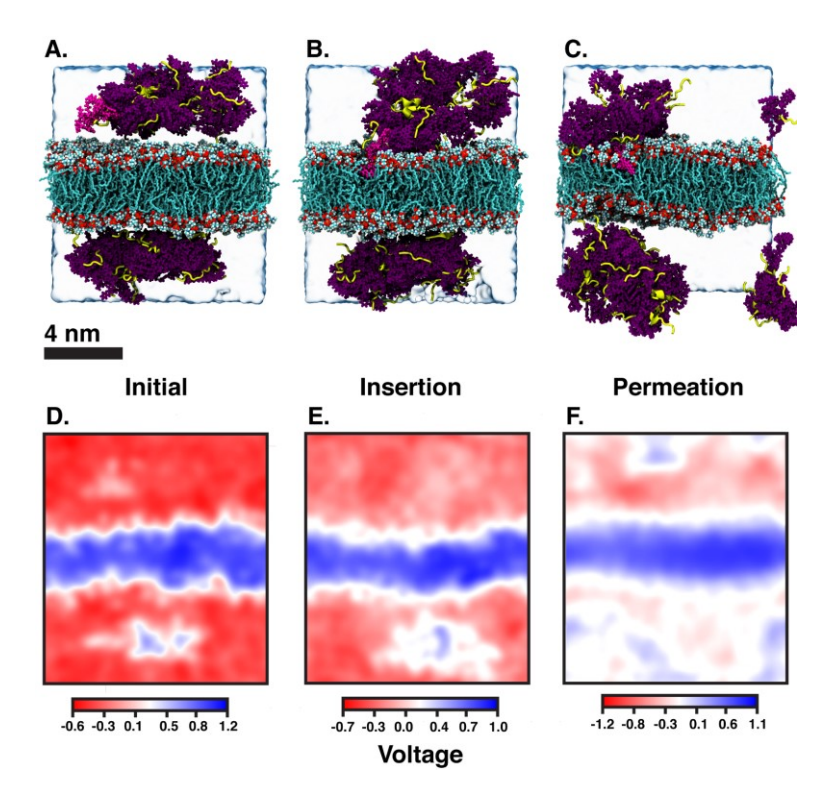


Figure 5. A-C. Snapshots show 'nanoclusters' of 'qCPT-buSS-Tau' interacting with the model POPC membrane at the A. Initial (0ns), B. Insertion (88 ns), and C. Permeation (25 μs) timepoints. Camtothecin (CPT) are in purple with Licorice presentation, peptides are yellow with secondary structure presentation. POPCs are shown in default colors (cyan, red, white) in 'Licorice' representation. Water is represented by a transparent box. CPT that inserts itself in the outer hydrophobic core of the membrane is highlighted in magenta. D-E. 2D Electrostatic potential maps after the Initial (0ns), Insertion (88 ns), and Permeation (25 μs) timepoints demonstrating the positively charged surface of the POPC membrane. The +ve potential and -ve potential are shown in blue and red respectively.

penetrate and insert in the membrane at ~ 100 ns with the dru 20 eventually stacking up at the membrane surface and permeating t 64 membrane as shown in Figure 5. Here, we identify two critic 20 events: Insertion at 88 ns and deeper partitioning of the drug into t 64 membrane or Permeation at 25 μs. In contrast to 'mCPT-buSS-Ta 34' after 6 μs, we do not observe an equilibrium state of the 'qCPT-buS3-5 Tau' nanoclusters, in terms of the average size or number 36 molecules per cluster, as shown in Supplemental Figure 1 C-37 Indeed, the average size still decreases after 25 μs as the number 38 nanoclusters is increasing. After the insertion event at 88 ns, t 649 original larger nanoclusters dissolve into smaller nanoclusters which is shown as a decrease of the average size from 10 to 6 in Figure 3.41 Also, the sphericity, which describes the overall shapes of the 'qCP42 buSS-Tau' nanoclusters, follows a different trend compared 463 'mCPT-buSS-Tau'.

As shown in **Figure 3 B**, small to medium nanoclusters of 'qCP45 buSS-Tau' have a similar sphericity index of ~ 0.5 as for the 'mCP46 buSS-Tau'. In other words, the overall shape of the small to mediu47 drug-amphiphilic peptides are ellipsoidal regardless of their chemic48 structures. Nevertheless, when qCPT nanoclusters reach more th49 ~ 0.5 normalized size, their sphericity index rapidly approaches 150 indicated they become rounder/more spherical. A positive line51 regression predicts this trend to be followed when a normalized si52 of 1 is reached. We postulate that such a spherical shape in larg53 qCPT nanoclusters may nucleate nanotube formation, which 54 observed in experiments³⁵. However, it is unclear what the role o65 membrane interface may play in facilitating self-assembly.

Next, we characterize the 2D free energy surface to investiga the relationship between the 'qCPT-buSS-Tau' nanocluster sizes a 58

the relative distance, d₂, between the nanocluster and the COM of the POPC bilayer. As mentioned, dz measures from the lowest point of each nanocluster (or closest atom (to the membrane?) in the nanocluster) to the COM of the membrane to characterize the penetration, or closest point of approach, of the drugs. From Figure **4 D**, we observe two 'qCPT-buSS-Tau' nanocluster populations: the first dominant population with ~ 0.1 normalized size (small to medium sizes), and the second population with ~ 0.5 normalized size (larger sizes). Initially, the first population is concentrated mostly at ~36 Å (0 kcal/mol) and at ~72 Å (1 kcal/mol) with its minimum d_z is at 24 Å while the second population is located at ~72 Å (~2.5 kcal/mol). Moreover, 'gCPT-buSS-Tau' nanoclusters are 12 Å closer to the membrane compared to 'mCPT-buSS-Tau'. One may argue that the initial random configurations favor a closer distance for 'qCPT-buSS-Tau' than 'mCPT-buSS-Tau', as shown in Figure 2 A and **5** A, respectively. Nevertheless, the 'Insertion' event at 88 ns has the minimum d_z of the first population of drugs that penetrate the membrane as deep as 12 Å; and at the end of the simulation, the penetration is at its deepest, which is only 6 Å away from the COM of the membrane, as shown in as shown in Figure 4 E-F. Visual inspection of Figure 5 B shows that only 8 CPT drugs, colored in magenta, diffuse past the outer head group layer. While there is clear membrane bending after 25 µs simulation (Figure 5 C), the local membrane thickness and the x-y positions of the drugs that position themselves in the outer hydrophobic core of the membrane are only weakly correlated, as shown in Supplemental Figure 2.

As mentioned, 'qCPT-buSS-Tau' nanoclusters break into smaller sizes after insertion but their clustering propensity is still high. In other words, after breaking apart, 'qCPT-buSS-Tau' nanoclusters

2

3

4

5

6

7

8

9

10

11

12

13

14

15

16

17

18

19

20

21

22

23

24

25

26

27

28

29

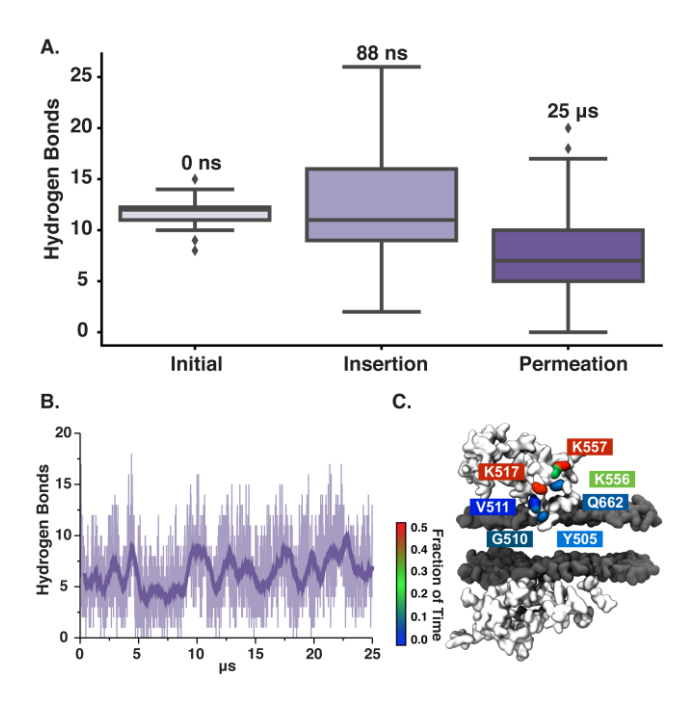


Figure 6. A. Total hydrogen bonds after the Initial (0 ns), Insertion (88 ns), and Permeation (25 μ s) timepoints. The lowest, middle, and top lines of the boxes are 25, 50, and 75 percentiles, respectively. The top and bottom lines are maxima and minima, with the outliers as black diamonds **B.** The average hydrogen bonds between 'qCPT-buSS-Tau' and the POPC bilayer during 25 μ s trajectory. The transparent line shows the raw data and the opaque line shown the running average over the previous 100 frames. **C.** The amino acid involved and the lifetime of the associated hydrogen bonds between nanoclusters of the 'qCPT-buSS-Tau' and the POPC membrane.

reorganize and form aggregates again. We hypothesize that there are competing free energy contributions between the *inter*- and *intra*- nanocluster interactions. In other words, the enthalpic interactions between the POPC and the 'qCPT-buSS-Tau' nanoclusters, specifically the camptothecin⁴³, are more favorable than the mainly hydrophobic and stacking interactions that hold the 'qCPT-buSS-Tau' nanoclusters together. As a result, the POPC membrane allows the 'qCPT-buSS-Tau' nanoclusters inside, leading via the hydrophobic CPT, breaking the larger aggregates.

1

2

3

4

5

6

7

8

9

10

11

12

13

14

15

16

17

18

19

20

21

22

23

24

25

When the DAs insert into the membrane, drug first, we hypothesize that the insertion may affect the overall electrostatics at the membrane interface. Since the peptides contain multiple positively charged Lysines, we expect to see a shift in the electrostatic potential along the z-direction of the membrane, as the peptides are pulled closer to the membrane surface. The choline and phosphate phospholipid head groups at the interface give the membrane surface a net dipole moment, with the positively charged cholines on the surface. Figure 5 D-F shows the electrostatic potential (EP) map that is calculated from the PMEPot⁶⁷ plugin in Visual Molecular Dynamics (VMD)⁶⁷ using fast Fourier transformations to solve Poisson's equation numerically. A detailed explanation can be found in Aksimentiev et al⁶⁸. Only a slice through the simulation box at the insertion site above and below the membrane surrounding the CPT drugs are shown. We find that the membrane is more positive than the surrounding water, which contains Cl-ions and is net negatively charged. The hydrophobic CPT drugs are buried inside the amphiphilic peptides. In the initial configuration, there is a net positive region (0.1 – 0.5 V) that appears in the surrounding water. This is attributed to the positively charged Lysines, that are mostly buried. However, after 25 μs , more Lysines are pointing outwards as multiple more positive regions (~ 1V) appear around the membrane in the surrounding water. However, this would in effect put a positively charged 'coat' on the qCPT nanoclusters. As a result, the net positive charge of the membrane surface may repulse this positively charged 'coat' on the qCPT nanoclusters. The interaction between the membrane surface and larger self-assemblies will be quantified in more detail in the next section.

We next observe that 'qCPT-buSS-Tau' nanoclusters anchor themselves above the membrane, while 'mCPT-buSS-Tau' nanoclusters fail to do so. Hydrogen bonds between the peptides and the membrane surface may play a crucial role in this anchoring step. In Figure 6 B, an average of 5-10 hydrogen bonds persistently exist between 'qCPT-buSS-Tau' nanoclusters and the membrane, while there is an average of only one hydrogen bond between 'mCPT-buSS-Tau' and the membrane (as shown in Supplemental Figure 3). Clearly, the multi-fold difference in hydrogen bonds between mCPT and qCPT reemphasizes the important role of the hydrogen bonds in forming an anchor for the nanoclusters above the membrane surface. Additionally, Figure 6 A shows a significant increase in hydrogen bonds formed during insertion, most of them lasting 25 μs. As the result, we calculate the lifetimes of hydrogen bonds between 'gCPT-buSS-Tau' nanoclusters and the POPC membrane. Hydrogen bond analysis was performed using the Cpptraj package⁶⁹ from AmberTools package. The cut-off angle between the hydrogen donor-hydrogen atom-hydrogen acceptor was 120°, and the cut-off distance between hydrogen donor-hydrogen acceptor was 3 Å. We

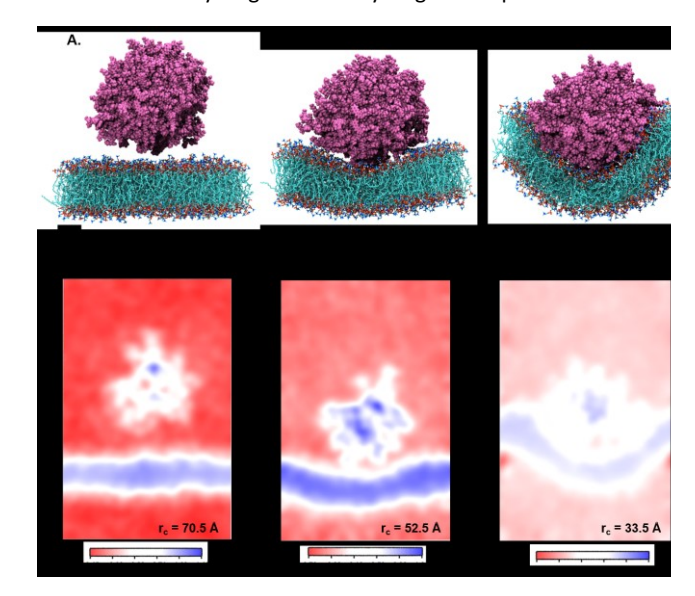


Figure 7. Snapshots from umbrella sampling calculations showing nanofilament interaction with the membrane at three reaction coordinates (r_c) selected when nanofilament is **A.** away from the membrane (r_c = 70.5 Å) **B.** approaching the membrane (r_c = 52.5 Å) and **C.** in contact with the membrane (r_c = 33.5 Å) . 2D Electrostatic potential maps for nanofilament interaction with the membrane when nanofilament is **D.** away from the membrane **E.** approaching the membrane and **F.** in contact with the membrane. The +ve potential and -ve potential are shown in blue and red respectively.

62

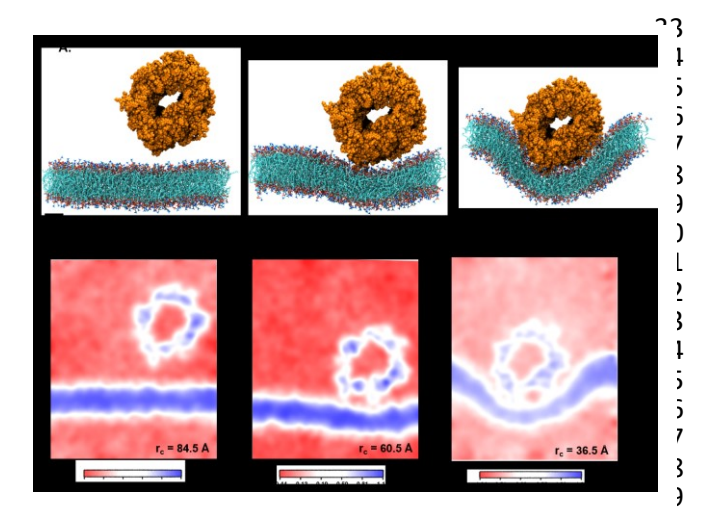


Figure 8. Snapshots from umbrella sampling calculations showing the nanotube interaction with the membrane at three reaction coordinates (r_c) selected when nanofilament is **A.** away from the membrane $(r_c = 84.5 \text{ Å})$ **B.** approaching the membrane $(r_c = 36.5 \text{ Å})$ and **C.** in contact with the membrane $(r_c = 36.5 \text{ Å})$. Electrostatic potential maps for nanotube interaction with the membrane when nanotube is **D.** away from the membrane **E.** approaching the membrane and **F.** in contact with the membrane. The +ve potential and -ve potential are shown in blue and red respectively.

considered all atoms on 'qCPT-buSS-Tau' and POPCs. In Figure 663 K517, K556, K557 have the most extended lifetimes spanning 30-5064 of the 25 us trajectory. G510 occurs during 10% of the trajecto 6/5 V511, Q662, Y505 are the least significant. K517 and G510 are on t66 same DA. K556 and K557 are on the same DA. V511, Q662, and Y567 are on different DAs. Both K517 and K557 are outer lysines in t68 peptide sequence. The rest of the residues, which are not show 69form extremely short lifetime hydrogen bonds with the membran 20 Surprisingly, we find a high density of persistent hydrogen bon d1 near the insertion site between the hydrophobic CPT and tage membrane. We hypothesize that 'qCPT-buSS-Tau' nanocluste 73 initially form scattered stable hydrogen bonds with the POFA membrane surface, effectively anchoring the nanoclusters to the surface of the membrane. Then, more stable hydrogen bon **a**6 aggregate, which can facilitate a high-density hydrogen bonding region on the surface of the nanoclusters. Eventually, the frace energy tips such that it becomes more favorable to break the nanoclusters apart, following by the reformation of su80 nanoclusters as several molecules leave and insert themselves in t84 82 membrane.

Umbrella Sampling.

4

5

6

7

8

9

10

11

12

13

14

15

16

17

18

19

20

21

22

23

24

25

27

28

29

30

31

Next, we perform umbrella sampling (US) to determine tset interaction energy of pre-assembled 'mCPT-buSS-Tau' nanofilamerses and 'qCPT-buSS-Tau' nanotubes with the POPC model membrarses are 7-A, B, C shows snapshots of three windows from the US 87 the nanofilament interaction with the POPC membrane for reactions coordinates (r_c) of 70.5 Å, 52.5 Å and 33.5 Å respectively. These three snapshots represent three events during US—when the nanofilameses away from the membrane, approaching the membrane, and 91 contact with the membrane. These snapshots clearly indicate tset changing structure of the membrane as the nanofilameses approaches it—initially the membrane bends and then wraps tset

nanofilament. We do not observe any penetration of the membrane by the nanofilament suggesting a strong repulsive interaction between the membrane and the nanofilament. Next, we look at the electrostatic potential (EP) map during the three events mentioned above (Figure 7 -C, D, E). The EP map is calculated in VMD⁶⁷ for the last 10 ns of the 28 ns simulation of each US window. In these maps, we observe the solvent is negatively charged (red), the nanofilament and the membrane are both positively charged (blue) and the surrounding water solution is neutral (white). The nanofilament is positively charged with protonated Lysines surrounding the periphery of the nanofilament. The system has been neutralized by Cl- ions. Thus, it makes the solvent more negatively charged compared to the membrane and the nanofilament. The POPC membrane is composed of zwitterionic phosphatidylcholines and we observe the membrane is positively charged compared to its surroundings. The electrostatic potential maps for three events shift as the nanofilament approach the membrane. We find that the nanofilament is most positive when it is approaching the membrane (Figure 7 E) compared to when the filament is away (Figure 7 D) or in contact (Figure 7 F) with the membrane. Similarly, Figure 8 shows the snapshots of the 'qCPT-buSS-Tau' nanotube interaction with the membrane and the corresponding EP maps. The rc's of the three events when the nanotube is away from the membrane, approaching the membrane, and in contact with the membrane are 84.5 Å, 60.5 Å and 36.5 Å respectively (Figure 8 -A, B, C). Similar to the nanofilament scenario, we find that as the nanotube approaches, the membrane starts bending and then wraps the nanotube. Furthermore, the EP maps of the nanotube interaction with the membrane is complementary to the trend of nanofilament interaction with the membrane. We find the nanotube and the membrane is positively charged (blue) and the solvent is negatively charged (Figure 8- D, E, F).

Figure 9 shows the resulting PMF profile determined by US for the interaction of the nanofilament and the nanotube with the membrane. We find similar trends for both systems –the interaction energy increases as the nanofilament/nanotube approaches the membrane. However, it is energetically less costly for the nanofilament compared to the nanotube to interact with the membrane. This suggests that the nanofilament succeeds in making a higher number of favorable interactions with the membrane compared to the nanotube with the membrane. We find that hydrogen bonds between the nanofilament/nanotube with the membrane is one of the major intermolecular interactions. Each DA has two lysines which forms the outer periphery of the nanofilament and the nanotube, creating direct contact between lysines and the membrane (Figure 10 -A, B). Since the nanofilament has a smaller radius ~4.5 nm compared to the nanotube of radius ~5.0 nm, the outer surface area per 10 nm length for the nanofilament ~283 nm² is smaller than the surface area of the nanotube ~321 nm². Thus, lysines are packed much more closely for the nanofilament than for the nanotube. The density profile (Figure S 4) of the last window from US further indicates that the phosphate head groups of the membrane and the Lysines of the nanofilament and the nanotube are overlapping. Using VMD, we calculate the number of hydrogen bonds between the nanofilament and the nanotube with the membrane for two events —when approaching, and when in contact with the membrane. As shown in Figure S 5, the average number of hydrogen bonds increases as the nanofilament/nanotube approaches and then contacts the membrane. For both events, the average number of hydrogen bonds is significantly greater for the nanofilament-membrane interaction compared to nanotubemembrane interaction. Next, we characterize the residues from the

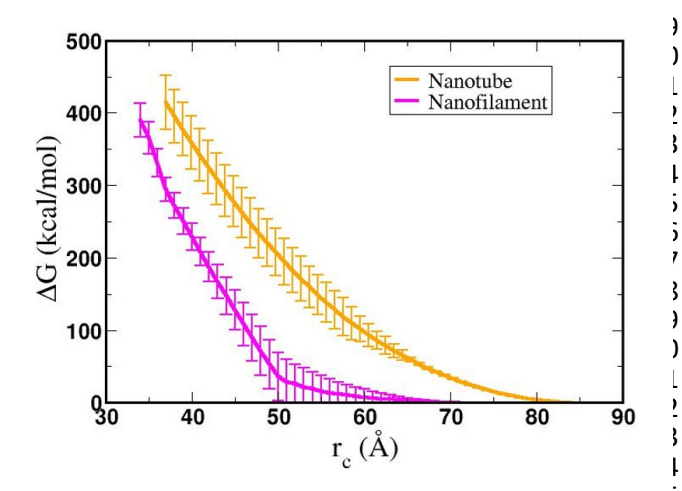


Figure 9. Free energy profile, ΔG (kcal/mol), calculated by umbrella sampling for the interaction of nanofilament (magenta) and nanotube (orange) with the POPC model membrane. The reaction coordinate (r_c) is the difference between center of mass (COM) of the membrane and the nanotube or the nanofilament, respectively.

1

3

4

5

6

7

8

9

10

11

12

13

14

15

16

17

18

19

20

21

22

23

24

25

26

27

28

29

30

31

33

34

35

36

37

nanofilament/nanotube forming hydrogen bonds with the membrane. For both systems, we find the number of hydrogen bonds for different residues of the nanofilament/ nanotube with the membrane is directly related to their position. As shown in Figure $\bar{\mathbf{B}}$ C, the average number of hydrogen bonds between lysines of the nanofilament and the nanotube with the membrane is significantly higher compared to tyrosines. Lysines being at the outer peripher $\check{\epsilon}\check{\gamma}$ of the nanofilament and the nanotube have direct contact with the membrane resulting in higher hydrogen bonds between lysines and the membrane. Tyrosine is the next inner residue after lysines in the DAs. Since tyrosines have less access to the membrane compared to lysines, the average number of hydrogen bonds between tyrosines and the membrane is significantly lower compared to the hydrogen bonds between lysines and the membrane. The fourth inner residue valine has negligible (~1) hydrogen bonds with the membrane for both systems. In Figure 10 D, we show the representative hydrogen bonds between lysine and membrane phosphate head groups. The greater hydrogen bonds of the nanofilament-membrane compared to nanotube-membrane supports the lower PMF for the nanofilament-membrane interaction compared to the nanotubemembrane interaction.

Next, we characterize structural changes in the membrane as the nanofilament/nanotube approaches the membrane surface. Figure 7 and 8 clearly show the membrane bending as the nanofilament/nanotube approaches. We calculate the change in thickness and surface area of the membrane during the three events previously described. The calculations are discussed in methods section. We find that the thickness of the membrane along the Y-axis decreases as the nanofilament/nanotube approaches and makes contact with the membrane. Figure 11-A, B shows the original membrane thickness of ~ 38 Å when the nanofilament/nanotube is far away from the membrane, which significantly decreases to the thickness of ~ 28 Å when the nanofilament/nanotube makes contact with the membrane. The change in thickness is dominant where the nanofilament/nanotube is in direct contact with the membrane (~ 10 Å thinner). Next, we calculate the surface area of the membrane during these three events (Figure 11 -C, D). We find the surface area of the membrane is greater for the membrane when in contact with the nanofilament/nanotube compared to when not in contact with the nanofilament/nanotube, with an increase of $^{\sim}$ 2000 Ų. The difference for the thickness and the surface area of the membrane is most significant between two end events — the nanofilament/nanotube away from the membrane and the nanofilament/nanotube in contact with the membrane. For the inner window, when the nanofilament/nanotube is approaching the membrane, the values of the membrane thickness are similar to the corresponding values when nanotube/nanofilament is further away from the membrane, while the surface area of the membrane has already increased. This suggests that the membrane first bends, without any contact with the nanofilament/nanotube, and then only thins upon contact.

Overall, using umbrella sampling, here we determine the interaction free energy of DA nanofilament and nanotube with a model POPC cell membrane. Membrane bending and wrapping of nanostructures of varying shapes has been characterized by coarse grained simulations of spherical nanoparticles and spherocylinders by Frenkel et al.⁷⁰ It is found that prolate shapes can lead to more efficient delivery. Here we find the interaction energy between the nanostructures and the membrane is very high (> 400 kcal/mol), suggesting that the process is energetically costly, but more costly for a nanotube vs. a nanofilament. We assume the bending rigidity k_c for a model POPC membrane and estimate the bending energy of the membrane, $F_{bend} = \frac{1}{2}k_cH^2$, where H is the mean curvature of the membrane. The bending energy of the membrane, F_{bend} , costs ~ 1/3 of the total interaction energy (~130 kcal/mol for the nanofilament system, and ~ 100 kcal/mol for the nanotube system), as described in the methods section. Previous computational studies by Liu et. al.71 have reported that clathrin-mediated endocytosis is easier for a softer membrane than a rigid membrane. These studies, conducted with varying membrane rigidity, found it is difficult for a rigid membrane to deform and form the vesicle necessary for

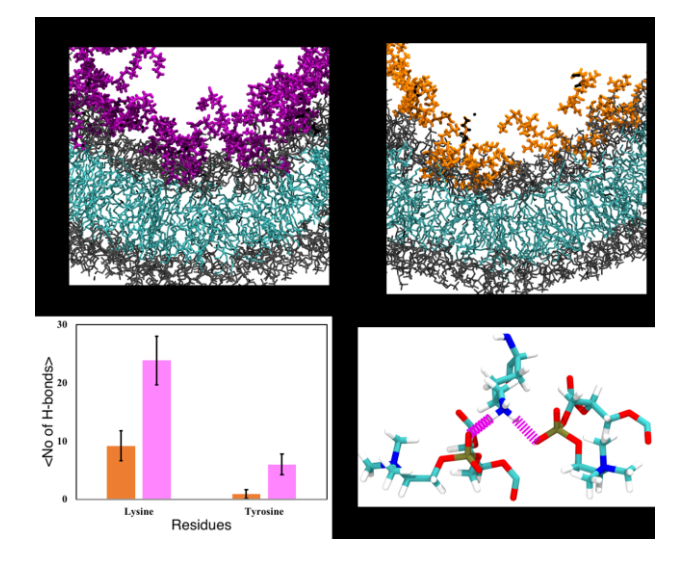


Figure 10. Interaction of Lysines of the A. nanofilament (magenta) and B. nanotube (orange) with model POPC membrane (head groups shown in gray and tail groups shown in cyan). C. Average no. of H-bonds formed by Lysines and Tyrosines of the nanofilament (magenta) and the nanotube (orange) with POPC membrane during last 10 ns of 28 ns simulation in the closest umbrella sampling window. D. Hydrogen bonds between the amine of the Lysine and Phosphate of the POPC head groups.

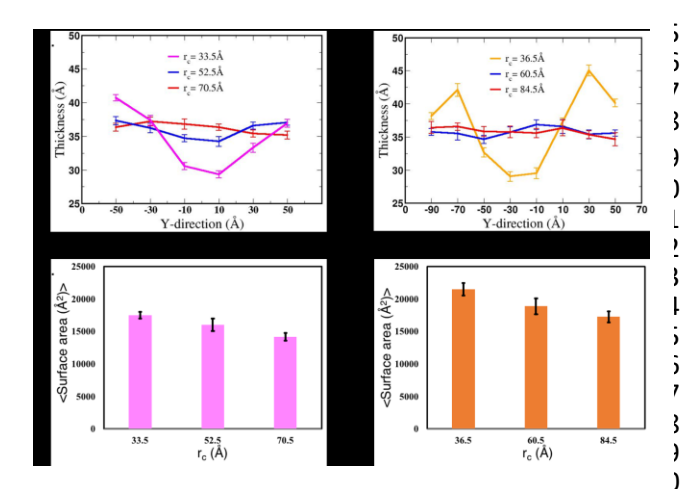


Figure 11. Thickness of the membrane during interaction with the A. nanofilament and B. nanotube. Average surface area of the membrane during interaction with the C. nanofilament and b. nanotube. These values are calculated for the last 10ns of the 28 ns simulation of the selected umbrella sampling windows. The thickness and average surface area for these systems are calculated at three timepoints—when the nanofilament/nanotube is away from the membrane, approaching membrane, and in contact with the membrane with decreasing r_values as shown above.

endocytosis⁷¹. However, this is a simplistic representation of the system and composition of the membrane as compared with a realistic membrane composition of the plasma membrane of the cancer cell. Notably, molecular dynamics simulations are moving towards more realistic phospholipid compositions to mimic representations. Significant differences have been observed in the interactions of cationic nanoparticles with zwitterionic vs. charged membranes computational studies by Cui et al.⁷³ have reported that cationic go nanoparticles have lower affinity to zwitterionic membranes by readily bind to 9:1 zwitterionic:anionic model membranes⁷³. Thus, including a range of anionically charged Phosphatidylserine (PS), to mimic the negative charge that is found in cancerous cells⁷⁴ may significantly modulate the degree of repulsion.

To summarize, the high interaction free energy, electrostate potential maps and the bending phenomena of the membrane indicate strong repulsive interaction between the nanostructures and the membrane. We find the interaction free energy of t7/4 nanofilament and the membrane is lower than the interaction free energy of the nanotube and the membrane. We suggest that one the factors contributing to this difference is the number of hydrogén bonds each nanostructure makes with the membrane. The nanofilament, having smaller radius than the nanotube, has a high lysine density on its surface facilitating more hydrogen bongs between the nanofilament and the membrane. During the simulations we did not observe pore formation in the membrane, not be served by the se significant deformation of the nanostructures. This suggests these nanostructures are very stable structures and to break these nanostructures into DAs will be energetically costly. Previous allatomistic and coarse-grained simulations of these anticancer nanostructures have shown these structures remain intact throughout simulations (~ microseconds), stabilized by $\pi^-\pi$ interactions between the DAs^{44, 52, 75, 76}. Thus, nanostructures will n**86** dissemble and release DAs and rather interact and traverse through the membrane as a one entity. Our observation of membrane

bending and wrapping of the nanostructures suggest endocytosis as the possible mechanism for the internalization of these nanostructures by the membrane.

Conclusions

Here, we report long-time molecular dynamics simulations (up to $25 \mu s$) to characterize how the DA structure affects the translocation across and interaction with the cellular membrane. Briefly, we find that DAs with lower drug loading (one drug attached per peptide) do not interact with or penetrate the membrane after very long timescales (18 µs). The results for a slightly different structure of the DA, four hydrophobic drugs attached per peptide, instead of only one drug attached, are strikingly different. In this case, due to the increased relative accessibility of the CPT, the hydrophobic cancer drug starts to interact with and penetrate the membrane after only 0.5 μs. After 25 μs we see that the drug builds up in a stacking configuration in the outer hydrophobic core of the membrane, starting to bend the membrane, pulling the positively charged peptide groups towards the membrane surface. Thus, singular DAs are suggested to interact with the membrane via a simple diffusive mechanism at shorter time-scales (< 1 microsecond), but, at longer timescales (≥ 10 µs) a more active mechanism. Next, using advanced sampling methods in molecular dynamics, we determine the potential energy of interaction of varying DA nanostructures—both nanofilament and nanotube—with the cell membrane. Here we find that both nanostructures repel the membrane due to their high positive surface charge density; however, the nanotube, with its increased diameter, is more repulsive. The membrane thins and bends as both nanostructures approach the membrane surface. Moreover, we find that hydrogen bonds between the nanostructure and the membrane may display a critical role in mediating membrane permeation. These results suggest that the interaction of engineered peptide sequences with model cellular membranes can be tailored through increasing the relative hydrophobicity of the molecule and through control of the hydrogen bond density between the nanostructure and membrane.

Conflicts of interest

There are no conflicts to declare.

Acknowledgements

S. M. L. acknowledges start-up funding received from College of Staten Island and City University of New York. S. M. L. would also like to acknowledge NSF Grant DMR-1750694 and support from the NIH (R15EB020343-01A1). A.M. would like to acknowledge partial support from the Rosemary O'Halleran scholarship. Anton 2 computer time was provided by the Pittsburgh Supercomputing Center (PSC) through Grant R01GM116961 from the National Institutes of Health. The Anton 2 machine at PSC was generously made available by D.E. Shaw Research.

Notes and references

References

2

5

6

7

8

9

10

11

12

13

14

15

16

17

18

19

20

21

22

23

24

25

26

27

28 29

30

31 32

33

1	1.	Y. Geng, P. Dalhaimer, S. Cai, R. Tsai, M. Tewari, T. Mink 63		G. E. Douberly, S. Pan, D. Walters and H. Matsui, Journal
2		and D. E. Discher, <i>Nature Nanotechnology</i> , 2007, 2 , 249-64		of Physical Chemistry B, 2001, 105 , 7612-7618.
3		255. 65		E. Vives, P. Brodin and B. Lebleu, <i>Journal of Biological</i>
4	2.	P. L. Rodriguez, T. Harada, D. A. Christian, D. A. Pantano, 66		Chemistry, 1997, 272 , 16010-16017.
5		R. K. Tsai and D. E. Discher, <i>Science</i> , 2013, 339 , 971-975.67		M. Green and P. M. Loewenstein, <i>Cell</i> , 1988, 55 , 1179-
6	3.	S. Mitragotri and J. Lahann, <i>Nature materials</i> , 2009, 8 , 1 6 8		1188.
7	4	23. 69 J. A. Champion and S. Mitragotri, <i>Proceedings of the</i> 70		V. P. Torchilin, <i>Advanced Drug Delivery Reviews</i> , 2008, 60 ,
8 9	4.			548-558.
9 10				C. Bechara and S. Sagan, <i>FEBS Letters</i> , 2013, 587 , 1693-
	5.	America, 2006, 103 , 4930-4934. 72 A. Verma, O. Uzun, Y. Hu, Y. Hu, HS. Han, N. Watson, S. 73		1702.
12	5.	Chen, D. J. Irvine and F. Stellacci, <i>Nature materials</i> , 200874		H. Brooks, B. Lebleu and E. Vivès, <i>Advanced Drug Delivery Reviews</i> , 2005, 57 , 559-577.
13		7 , 588-595.		A. D. Frankel and C. O. Pabo, <i>Cell</i> , 1988, 55 , 1189-1193.
	6.	M. Massignani, C. LoPresti, A. Blanazs, J. Madsen, S. P. 76		P. Zhang, A. G. Cheetham, L. L. Lock and H. Cui, <i>Bioconjug</i>
15	0.	Armes, A. L. Lewis and G. Battaglia, <i>Small</i> , 2009, 5 , 2424 77	54.	Chem, 2013, 24 , 604-613.
16		2432. 78	35.	A. G. Cheetham, P. Zhang, Y. A. Lin, L. L. Lock and H. Cui,
	7.	M. Kang and S. M. Loverde, <i>J Phys Chem B</i> , 2014, 118 , 79	33.	Journal of the American Chemical Society, 2013, 135 ,
18	, ·	11965-11972. 80		2907-2910.
	8.	N. J. Yang and M. J. Hinner, <i>Journal</i> , 2015, 1266 , 29-53. 81		W. J. Goux, L. Kopplin, A. D. Nguyen, K. Leak, M.
	9.	J. Wang, N. Lapinski, X. F. Zhang and A. Jagota, bioRxiv, 82		Rutkofsky, V. D. Shanmuganandam, D. Sharma, H. Inouye
21		2020, DOI: 10.1101/2020.06.26.173567, 83		and D. A. Kirschner, Journal of Biological Chemistry, 2004,
22		2020.2006.2026.173567.		279 , 26868-26875.
23	10.	D. J. Smith, L. G. Leal, S. Mitragotri and M. S. Shell, Journ85		M. D. Weingarten, A. H. Lockwood, S. Y. Hwo and M. W.
24		of Physics D-Applied Physics, 2018, 51 .		Kirschner, Proceedings of the National Academy of
	11.	A. Jusufi, R. H. DeVane, W. Shinoda and M. L. Klein, Soft 87		Sciences of the United States of America, 1975, 72 , 1858-
26		Matter, 2011, 7 , 1139-1146.		1862.
27	12.	X. B. Lin, Y. Li and N. Gu, Journal of Computational and 89	38.	G. Saito, J. A. Swanson and KD. Lee, Advanced Drug
28		<i>Theoretical Nanoscience</i> , 2010, 7 , 269-276.		Delivery Reviews, 2003, 55 , 199-215.
29	13.	S. M. Loverde, M. L. Klein and D. E. Discher, Advanced 91	39.	E. A. Dubikovskaya, S. H. Thorne, T. H. Pillow, C. H. Contag
30		Materials, 2012, 24 , 3823-3830.		and P. A. Wender, <i>Proceedings of the National Academy</i>
31	14.	J. Q. Lin and A. Alexander-Katz, Acs Nano, 2013, 7, 1079 93		of Sciences of the United States of America, 2008, 105 ,
32		10808. 94		12128-12133.
33	15.	R. C. Van Lehn, P. U. Atukorale, R. P. Carney, Y. S. Yang, 195	40.	A. Manandhar, M. Kang, K. Chakraborty, P. K. Tang and S.
34		Stellacci, D. J. Irvine and A. Alexander-Katz, Nano Letters 96		M. Loverde, Organic & Biomolecular Chemistry, 2017, 15,
35		2013, 13 , 4060-4067. 97		7993-8005.
36	16.	J. D. Hartgerink, <i>Science</i> , 2001, 294 , 1684-1688.		M. E. Wall, M. C. Wani, C. E. Cook, K. H. Palmer, A. T.
37	17.	T. Aida, E. W. Meijer and S. I. Stupp, <i>Science</i> , 2012, 335 , 99		McPhail and G. A. Sim, Journal of the American Chemical
38		813-817. 100		Society, 1966, 88 , 3888-3890.
39	18.	T. Gore, Y. Dori, Y. Talmon, M. Tirrell and H. Bianco-Pel £0,1		A. Leo, C. Hansch and D. Elkins, <i>Chemical Reviews</i> , 1971,
40		Langmuir, 2001, 17 , 5352-5360. 102		71 , 525-616.
41	19.	H. Cui, M. J. Webber and S. I. Stupp, <i>Biopolymers</i> , 2010103		P. K. Tang, K. Chakraborty, W. Hu, M. Kang and S. M.
12		94, 1-18.		Loverde, Journal of Chemical Theory and Computation,
43 4.4	20.	E. Kokkoli, A. Mardilovich, A. Wedekind, E. L. Rexeisen, 105	4.4	2020, 16 , 3373-3384.
14 1	24	Garg and J. A. Craig, <i>Soft Matter</i> , 2006, 2 , 1015-1024. 106		M. Kang, P. Zhang, H. Cui and S. M. Loverde,
45 46	21.	J. D. Hartgerink, E. Beniash and S. I. Stupp, <i>Proceedings</i> 107		Macromolecules, 2016, 49 , 994-1001.
46 47		the National Academy of Sciences of the United States 108 America, 2002, 99 , 5133-5138.	45.	S. Jo, T. Kim, V. G. Iyer and W. Im, <i>J Comput Chem</i> , 2008, 29 , 1859-1865.
+7 48	22	America, 2002, 99 , 5133-5138. 109 A. Dehsorkhi, V. Castelletto and I. W. Hamley, <i>Journal of</i> 1	46.	C. J. Dickson, B. D. Madej, A. A. Skjevik, R. M. Betz, K.
+0 19	22.	peptide science: an official publication of the European 111		Teigen, I. R. Gould and R. C. Walker, <i>J Chem Theory</i>
50		Peptide Society, 2014, 20 , 453-467. 112		Comput, 2014, 10 , 865-879.
51	23.	X. Zhao, Y. Nagai, P. J. Reeves, P. Kiley, H. G. Khorana a 1d3		J. C. Phillips, R. Braun, W. Wang, J. Gumbart, E.
52	23.	S. Zhang, <i>Proceedings of the National Academy of</i> 114		Tajkhorshid, E. Villa, C. Chipot, R. D. Skeel, L. Kale and K.
53		Sciences, 2006, 103 , 17707-17712.		Schulten, <i>J Comput Chem</i> , 2005, 26 , 1781-1802.
54	24.	K. Matsumoto, M. Vaughn, B. D. Bruce, S. Koutsopoulo 116		G. J. Martyna, D. J. Tobias and M. L. Klein, <i>The Journal of</i>
55		and S. Zhang, Journal of Physical Chemistry B, 2009, 113,17	10.	Chemical Physics, 1994, 101 , 4177-4189.
56		75-83. 118	49.	S. E. Feller, Y. Zhang, R. W. Pastor and B. R. Brooks, <i>The</i>
57	25.	G. A. Silva, C. Czeisler, K. L. Niece, E. Beniash, D. A. 119		Journal of Chemical Physics, 1995, 103 , 4613-4621.
58		Harrington, J. A. Kessler and S. I. Stupp, <i>Science</i> , 2004, 120		J. Wang, R. M. Wolf, J. W. Caldwell, P. A. Kollman and D.
59		303 , 1352-1355. 121		A. Case, Journal of Computational Chemistry, 2004, 25 ,
50	26.	Y. A. Lin, A. G. Cheetham, P. Zhang, Y. C. Ou, Y. Li, G. Liu, 22		1157-1174.
51		D. Hermida-Merino, I. W. Hamley and H. Cui, ACS Nand 23		L. Martinez, R. Andrade, E. G. Birgin and J. M. Martinez, J
52		2014, 8 , 12690-12700.		Comput Chem, 2009, 30 , 2157-2164.

- M. Kang, K. Chakraborty and S. M. Loverde, Journal of 63 1 52. 2 Chemical Information and Modeling, 2018, 58, 1164-1168.
- 3 53. I. Y. B.-S. D.A. Case, S.R. Brozell, D.S. Cerutti, T.E.
- 4 Cheatham, III, V.W.D. Cruzeiro, T.A. Darden, R.E. Duke, D. 5 Ghoreishi, M.K. Gilson, H. Gohlke, A.W. Goetz, D. Greene,
- 6 R Harris, N. Homeyer, S. Izadi, A. Kovalenko, T. Kurtzman, 7
 - T.S. Lee, S. LeGrand, P. Li, C. Lin, J. Liu, T. Luchko, R. Luo,
- 8 D.J. Mermelstein, K.M. Merz, Y. Miao, G. Monard, C.
- 9 Nguyen, H. Nguyen, I. Omelyan, A. Onufriev, F. Pan, R. Qi,
- 10 D.R. Roe, A. Roitberg, C. Sagui, S. Schott-Verdugo, J. Shen,
- 11 C.L. Simmerling, J. Smith, R. Salomon-Ferrer, J. Swails, R.C.
- 12 Walker, J. Wang, H. Wei, R.M. Wolf, X. Wu, L. Xiao, D.M. 13 York and P.A. Kollman, Amber18, http://ambermd.org/).
- 14 54. H. C. Andersen, Journal of Computational Physics, 1983,
- 15 **52**, 24-34.
- 16 55. T. Darden, D. York and L. Pedersen, The Journal of 17 Chemical Physics, 1993, 98, 10089-10092.
- 18 56. D. E. Shaw, J. Grossman, J. A. Bank, B. Batson, J. A. Butts,
- 19 J. C. Chao, M. M. Deneroff, R. O. Dror, A. Even and C. H. 20 Fenton, 2014.
- 21 Y. Shan, J. L. Klepeis, M. P. Eastwood, R. O. Dror and D. E. 57. 22 Shaw, J Chem Phys, 2005, 122, 54101.
- 23 58. G. M. Torrie and J. P. Valleau, Journal of Computational 24 Physics, 1977, 23, 187-199.
- 25 59. W. S. Young and C. L. Brooks Iii, Journal of Molecular 26 Biology, 1996, 259, 560-572.
- 27 60. B. D. Bursulaya and C. L. Brooks, Journal of the American 28 Chemical Society, 1999, 121, 9947-9951.
- 29 61. R. Vijayaraj, S. Sundar Raman, R. Mahesh Kumar and V. 30 Subramanian, The Journal of Physical Chemistry B, 2010, 31 **114**. 16574-16583.
- 32 62. S. Mahdavi and S. Kuyucak, Biochemistry, 2013, 52, 1631-33
- 34 63. D. Yesudhas, M. A. Anwar, S. Panneerselvam, H. K. Kim 35 and S. Choi, FEBS Open Bio, 2017, 7, 1750-1767.
- 36 64. S. Nangia, J. G. Pattis and E. R. May, Journal of Biological 37 Physics, 2018, 44, 195-209.
- 38 65. S. Kumar, J. M. Rosenberg, D. Bouzida, R. H. Swendsen 39 and P. A. Kollman, Journal of Computational Chemistry, 40 1992, **13**, 1011-1021.
- 41 B. Isralewitz, J. Baudry, J. Gullingsrud, D. Kosztin and K. 66.
- 42 Schulten, J Mol Graph Model, 2001, 19, 13-25.
- 43 67. W. Humphrey, A. Dalke and K. Schulten, Journal of 44 Molecular Graphics, 1996, 14, 33-38.
- 45 68. A. Aksimentiev and K. Schulten, Biophys J, 2005, 88, 3745-46 3761.
- 47 69. D. R. Roe and T. E. Cheatham, 3rd, J Chem Theory Comput,
- 48 2013, **9**, 3084-3095. 49 70. R. Vacha, F. J. Martinez-Veracoechea and D. Frenkel, Nano
- 50 Letters, 2011, 11, 5391-5395.
- 51 71. H. Deng, P. Dutta and J. Liu, Biochimica et Biophysica Acta 52 - General Subjects, 2018, 1862, 2104-2111.
- 53 72 S. J. Marrink, *Biophysical Journal*, 2018, **114**, 367A-367A.
- 54 73. M. Das, U. Dahal, O. Mesele, D. Liang and Q. Cui, Journal 55 of Physical Chemistry B, 2019, 123, 10547-10561.
- 56 74. C. R. T. Rivel, S. O. Yesylevskyy, DOI:
- 57 https://doi.org/10.1101/375980.
- 58 M. Kang, H. Cui and S. M. Loverde, Soft Matter, 2017, 13, 75. 59
- 60 76. A. Manandhar, K. Chakraborty, P. K. Tang, M. Kang, P.
- 61 Zhang, H. Cui and S. M. Loverde, Journal of Physical
- 62 Chemistry B, 2019, 123, 10582-10593.